Unconventional angular dependence of spin-orbit torque-induced harmonic Hall resistance in Pt/YIG bilayers

Byong-Guk Park

bgpark@kaist.ac.kr

KAIST

Takayuki Shiino
KAIST

Cao Van Phuoc
Chungnam National University

Jong-Guk Choi
KAIST

Geunwoo Kim
KAIST

Jong-Ryul Jeong
Department of Material Science and Engineering and Graduate School of Energy Science and Technology, Chungnam National University, Daejeon 34134

Additional Declarations: No competing interests reported.

Unconventional angular dependence of spin-orbit torque-induced harmonic Hall resistance in Pt/YIG bilayers

Takayuki Shiino[1], Phuoc Cao Van[2], Jong-Guk Choi[1], Geunwoo Kim[1], Jong-Ryul Jeong[2], and Byong-Guk Park[1]*

[1]*Department of Materials Science and Engineering, KAIST, Daejeon 34141, Republic of Korea*

[2]*Department of Material Science and Engineering, Chungnam National University, Daejeon 34134, Republic of Korea*

Abstract

Spin orbit torque (SOT), arising from spin-orbit coupling-induced spin currents, provides efficient control of the magnetization direction. SOT characterization that involves analyzing the first and second harmonic Hall resistances are typically done in a low-current regime, distinct from a high-current regime, where SOT-induced magnetization switching occurs. In this study, we investigate the azimuthal angle (ϕ)-dependent harmonic Hall resistances of a Pt/yttrium iron garnet (YIG) layer across a wide range of measurement currents. Under low-current conditions, conventional ϕ-dependent Hall resistances are observed; the first harmonic Hall resistance exhibits $\sin 2\phi$ behavior and the second harmonic Hall resistance comprises $\cos \phi$ and $\cos 3\phi$ terms, associated with damping-like and field-like SOT, respectively. Interestingly, with an increase in the current, higher-order angular-dependent terms become non-negligible, referring to the $\sin 4\phi$ and $\sin 6\phi$ terms for the first

harmonic and the $\cos 5\phi$ and $\cos 7\phi$ terms for the second harmonic Hall resistances. We attribute this unconventional angular dependence to the nonlinear current dependence of SOT, emphasizing its relevance to understand the magnetization dynamics during SOT-induced switching under large currents.

Spin-orbit torque (SOT), a type of spin torque caused by spin-orbit coupling-induced spin currents [1-3], enables the efficient electrical manipulation of magnetization in various spintronic devices. In particular, SOT provides a fast and energy-efficient means by which to realize current-induced magnetization switching [4,5] and domain wall motion [6,7], both of which can be exploited for magnetic random-access memory [8,9], spin Hall nano-oscillators [10,11], true random number generators [12], magnonic devices [13], and neuromorphic computing devices [14], among others. When applying a charge current in a typical heavy-metal (HM)/ferromagnet (FM) heterostructure, there are two main mechanisms responsible for SOT. The first is the spin Hall effect, generating a transverse spin current in the HM layer [2,15]. The second is the Rashba-Edelstein effect, inducing spin accumulation at the HM/FM interface with broken inversion symmetry [16,17]. These effects cause spin torque and control the magnetization direction. Various materials, including HMs [2,18] and their alloys [19,20], Weyl semimetals [21,22], and topological insulators [23-25], have been investigated as spin current sources, along with their combinations with FM (or antiferromagnetic) materials, as part of the effort to pursue high charge-to-spin conversion efficiency [1].

The characterization of SOT is a pivotal task in the development of SOT materials in spintronic applications. One of the most widely used methods to determine the magnitude and direction of SOTs is to analyze the first and second harmonic Hall resistances ($R_{xy}^{1\omega}$ and $R_{xy}^{2\omega}$) [2,26]. When an AC current $J = J_0 \sin \omega t$ is applied to the HM/FM heterostructure, SOTs induces magnetization oscillation with a modulation amplitude of ($\Delta\theta$, $\Delta\phi$) from the corresponding equilibrium direction (θ, ϕ) under an

external magnetic field, where J_0 and ω are the amplitude and angular frequency of the AC current density, and θ and ϕ are the polar and azimuthal angles of magnetization, respectively (see Fig. 1a). $R_{xy}^{1\omega}$ indicates the magnetization direction through the planar Hall effect (PHE, R_{PHE}) and anomalous Hall effect (AHE, R_{AHE}), while $R_{xy}^{2\omega}$ is mainly caused by the oscillation of magnetization due to SOT[27–29]. For FM with in-plane magnetization, as studied here, $R_{xy}^{1\omega}$ and $R_{xy}^{2\omega}$ can be described in terms of the azimuthal angle ϕ only (see details in the Supplementary Information S1),

$$R_{xy}^{1\omega} = c_{2\phi}^{1\omega} \sin(2\phi) + c_{4\phi}^{1\omega} \sin(4\phi) + c_{6\phi}^{1\omega} \sin(6\phi) + c_{8\phi}^{1\omega} \sin(8\phi) + \cdots, \quad (1)$$

$$R_{xy}^{2\omega} = c_{1\phi}^{2\omega} \cos(\phi) + c_{3\phi}^{2\omega} \cos(3\phi) + c_{5\phi}^{2\omega} \cos(5\phi) + c_{7\phi}^{2\omega} \cos(7\phi) + \cdots. \quad (2)$$

Here, $c_{2k\phi}^{1\omega}$ and $c_{(2k-1)\phi}^{2\omega}$ (where $k = 1,2,3,4$) are the current- and field-dependent coefficients (Supplementary Information S1). Note that we ignore higher-order terms ($k > 4$) in this study. Given that $R_{xy}^{1\omega}$ ($R_{xy}^{2\omega}$) is an even (odd) function with respect to J_0, $R_{xy}^{1\omega}$ ($R_{xy}^{2\omega}$) contains only even (odd)-number $n\phi$ symmetric terms (Supplementary Information S2). In a small current regime where higher-order terms are neglected, $R_{xy}^{1\omega}$ ($R_{xy}^{2\omega}$) exhibits $\sin 2\phi$ ($\cos \phi$ and $\cos 3\phi$) behavior, leading to the following equations,

$$R_{xy}^{1\omega} = R_{\text{PHE}} \sin 2\phi, \quad (3)$$

$$R_{xy}^{2\omega} = \left(R_{xy}^{\text{SSE}} + R_{\text{AHE}} \frac{H_{\text{DL}}}{2H_{\text{eff}}} \right) \cos \phi + R_{\text{PHE}} \frac{H_{\text{FL}} + H_{\text{Oe}}}{H_{\text{a}}} (2 \cos^3 \phi - \cos \phi), \quad (4)$$

where $c_{2\phi}^{1\omega} \approx R_{\text{PHE}}$, $c_{1\phi}^{2\omega} \approx R_{xy}^{\text{SSE}} + \frac{R_{\text{AHE}}H_{\text{DL}}}{2H_{\text{eff}}} + \frac{R_{\text{PHE}}}{2} \frac{H_{\text{FL}} + H_{\text{Oe}}}{H_{\text{a}}}$, and $c_{3\phi}^{2\omega} \approx \frac{R_{\text{PHE}}}{2} \frac{H_{\text{FL}} + H_{\text{Oe}}}{H_{\text{a}}}$; H_{eff} is the effective field including the applied field H_{a} and the demagnetization and anisotropy fields of the FM layer, and H_{DL}, H_{FL}, and H_{Oe} are the damping-like (DL) and field-like (FL) effective fields of the

4

SOT and Oersted fields, respectively. R_{xy}^{SSE} is the spin Seebeck effect (SSE) contribution. Note that these equations have been widely employed to characterize SOTs in various materials systems [30–33]. We want to emphasize that the characterization of SOT using harmonic Hall resistance measurements has mainly been done in a low-current regime as opposed to the high-current regime in which SOT-induced magnetization switching occurs. A recent study[34] reported the measurement of high-order angular dependence in the third harmonic Hall resistance of Pt/α-Fe$_2$O$_3$ at a current density of 1.6×10^{11} A/m^2. This was attributed to the DL SOT of the sample, where the DL SOT terms in the second harmonic Hall resistance $R_{xy}^{2\omega}$ are canceled out due to the alternating antiferromagnetic moments of α-Fe$_2$O$_3$. This result suggests that the higher-order angular-dependent terms in Eqs. (1) and (2) may appear in a high-current regime even in FM, which is the main theme of this study.

Here, we report a systematic study of azimuthal angle (ϕ)-dependent harmonic Hall resistances in a Pt/yttrium iron garnet (Y$_3$Fe$_5$O$_{12}$: YIG) layer investigated under a wide range of measurement currents. Under low-current conditions, we observed conventional ϕ-dependent behavior in $R_{xy}^{1\omega}$ and $R_{xy}^{2\omega}$, well described by Eqs. (3) and (4), respectively. On the other hand, as the current increases, the ϕ dependencies of $R_{xy}^{1\omega}$ and $R_{xy}^{2\omega}$ deviate significantly from the corresponding conventional shapes. This is evidenced by the saw-tooth-wave-like (in $R_{xy}^{1\omega}$) and the square-wave-like (in $R_{xy}^{2\omega}$) curves, where the higher-order terms become non-negligible. For example, at a current density of $J_0 = 2 \times 10^{11}$ A/m^2, the magnitude of the 4ϕ (5ϕ) term of $R_{xy}^{1\omega}$ ($R_{xy}^{2\omega}$) can be as high as 30% (20%) of that of the lowest 2ϕ (1ϕ) term. We attribute this unconventional ϕ-dependence of $R_{xy}^{1\omega}$ and $R_{xy}^{2\omega}$

to nonlinear current-dependent SOTs. This result will contribute to advancing the understanding of magnetization dynamics during the SOT-induced switching of magnetization under large currents.

Harmonic Hall resistances in a low-current regime

First, we check the conventional behaviors of $R_{xy}^{1\omega}$ and $R_{xy}^{2\omega}$ in a Pt (3 nm)/YIG (30 nm) layer in a low-current regime ($J_0 < 1 \times 10^{11}$ A/m^2). Here, YIG film was grown on a GGG (111) substrate by means of RF sputtering at room temperature, followed by a post-annealing step at 750 °C in an oxygen environment for two hours. Details of the sample growth conditions are provided in the Methods section. The grown YIG film exhibits good crystallinity well matched to the GGG substrate (Supplementary Information S3) and in-plane magnetic anisotropy (Supplementary Information S4). Figure 1b shows an image of the Hall bar device. Figures 1c and 1d show the $R_{xy}^{1\omega}$ and $R_{xy}^{2\omega}$ of the sample measured at a current density of 8.3×10^{10} A/m^2 with different magnetic fields (H_a). Note that even in a Pt/YIG film with an insulating FM, where the current flows only in the non-magnetic Pt, $R_{xy}^{1\omega}$ depends on the magnetization direction of YIG due to the spin Hall magnetoresistance[27,35], the magnetic proximity effect in Pt[36–38], and interfacial spin-dependent scattering[39]. Note that the angular dependence of the longitudinal resistances of the sample was also measured, corresponding to spin Hall magnetoresistance (unidirectional spin Hall magnetoresistance) with a magnitude of 0.036% (2.3×10^{-4} %) at $J_0 = 1 \times 10^{11}$ A/m^2 and $H_a = 25$ Oe for the first (second) harmonic resistance (Supplementary Information S5). Figure 1c shows the angular dependence of $R_{xy}^{1\omega}$, identical in all

cases regardless of the magnitude of H_a and thus exhibiting typical $\sin 2\phi$ behavior of PHE. On the other hand, Figure 1d shows the angular dependence of $R_{xy}^{2\omega}$, demonstrating clear dependence on H_a. This is expected from Eq. (4), indicating that the H_a contribution to $R_{xy}^{2\omega}$ overtakes that of the SOT-induced effective fields (H_{DL}, H_{FL}) for a large H_a. To obtain H_{DL} and H_{FL}, we separated the $\cos\phi$ and $[2\cos^3\phi - \cos\phi]$ components and then plotted the extracted $R_{\cos\phi}^{2\omega}$ and $R_{[2\cos^3\phi-\cos\phi]}^{2\omega}$ values as a function of $1/H_{eff}$ and $1/H_a$, respectively (Figs. 1e, f). From the slopes of the $R_{\cos\phi}^{2\omega}$ and $R_{[2\cos^3\phi-\cos\phi]}^{2\omega}$ versus $1/H_{eff}$ and $1/H_a$ curves, the values of $(H_{FL} + H_{Oe}) = 0.93$ Oe, $H_{DL} = 10.1$ Oe were extracted at $J_0 = 1 \times 10^{11}$ A/m^2. Note that we obtained a value of $R_{AHE} = 2.7$ mΩ (Supplementary Information S6) and the y-intercept of the $R_{\cos\phi}^{2\omega}$ vs $1/H_{eff}$ plot (Fig. 1e) indicates the SSE component (R_{xy}^{SSE}). These behaviors are consistent with those in the previous reports[30].

Harmonic Hall resistances in a high-current regime

Next, we examined the angular dependence of $R_{xy}^{1\omega}$ and $R_{xy}^{2\omega}$ in the high-current regime, exhibiting behaviors different from those in low-current regimes. Figures 2a and 2b display the results measured for three different current densities, $J_0 = 0.5,\ 1.0,$ and 2.2×10^{11} A/m^2 Here, $H_a = 25$ Oe. As the current increases, the ϕ dependencies of $R_{xy}^{1\omega}$ and $R_{xy}^{2\omega}$ deviate significantly from the conventional shapes shown in Fig. 1. Interestingly, they started to resemble saw-tooth wave form (in $R_{xy}^{1\omega}$) and square-wave form (in $R_{xy}^{2\omega}$) curves at $J_0 \sim 2.2 \times 10^{11}$ A/m^2, which cannot be explained

using Eqs. (3) and (4). Therefore, to account for the experimental data, we used Eqs. (1) and (2). The decomposed $n\phi$ $(n = 1, 2, ..., 8)$ angular-dependent curves are indicated by the colored lines in Figs. 2a and 2b. Notably, as the current increases, the higher-order angular components of 4ϕ, 6ϕ and 8ϕ (5ϕ and 7ϕ) in $R_{xy}^{1\omega}$ ($R_{xy}^{2\omega}$) becomes non-negligible, indicating that higher-order terms should be considered when analyzing SOT-induced harmonic Hall resistances.

To gain a quantitative understanding of the higher-order terms, we repeated the harmonic Hall resistance measurements under various current levels ($0.5 \times 10^{11} \leq J_0 \leq 2.2 \times 10^{11}$ A/m^2) and magnetic fields (25 Oe $\leq H_a \leq$ 10 kOe) [Supplementary Information S7]. Figures 2c and 2d display the absolute values of the lowest-order unconventional angular-dependent coefficients, $\left|c_{4\phi}^{1\omega}\right|$ and $\left|c_{5\phi}^{2\omega}\right|$ (normalized by the leading terms $\left|c_{2\phi}^{1\omega}\right|$ and $\left|c_{1\phi}^{2\omega}\right|$, respectively) as functions of J_0 and H_a. These results demonstrate that the magnitudes of $\left|c_{4\phi}^{1\omega}\right|$ and $\left|c_{5\phi}^{2\omega}\right|$ become significant under large currents and small external fields, where saw-tooth-wave-like (in $R_{xy}^{1\omega}$) and square-wave-like (in $R_{xy}^{2\omega}$) angular-dependent curves are observed in Figs. 2a and 2b. Note that these $\left|c_{4\phi}^{1\omega}\right|$ and $\left|c_{5\phi}^{2\omega}\right|$ values are suppressed as H_a increases, suggesting that they originate from the SOT-induced magnetization oscillation. The magnitude of $\left|c_{4\phi}^{1\omega}\right|$ ($\left|c_{5\phi}^{2\omega}\right|$) can reach about 30% (20%) of that of the leading term $\left|c_{2\phi}^{1\omega}\right|$ ($\left|c_{1\phi}^{2\omega}\right|$) at $J_0 \sim 2 \times 10^{11}$ A/m^2. These unconventional angular-dependent $n\phi(n \geq 4)$ terms ultimately changed the angular dependence of $R_{xy}^{1\omega}$ and $R_{xy}^{2\omega}$.

Figure 3 shows the current dependence of the coefficients $c_{n\phi}^{2\omega}$ $(n = 1, 3, 5, 7)$ in $R_{xy}^{2\omega}$ at $H_a =$ 25 Oe obtained by fitting the $R_{xy}^{2\omega}$ data to Eq. (2). We found that the signs of $c_{3\phi}^{2\omega}$, $c_{5\phi}^{2\omega}$ and $c_{7\phi}^{2\omega}$

change with an increase in J_0. This sign reversal can be attributed to the nonlinear current dependence

of SOT. For example, $c_{5\phi}^{2\omega}$ can be described as $c_{5\phi}^{2\omega} = -A_1 J_0^3 + A_2 J_0^5 + \cdots$, where A_1 and A_2 are

the coefficients of the SOT effective fields. The details about A_1 and A_2 are found in Supplementary

Information 1. The sign of $c_{5\phi}^{2\omega}$ changes when the second term A_2 (proportional to J_0^5) becomes

larger than the first term A_1 (proportional to J_0^3) under a large current. Likewise, the higher-order

current dependence causes sign changes of the other coefficients $c_{3\phi}^{2\omega}$ and $c_{7\phi}^{2\omega}$ as well [see Eqs. S16

and S18 in Supplementary Information S1].

Discussion

Finally, we discuss the implications of the present results; i.e., the unconventional $n\phi$ ($n \geq 4$)

angular dependence of $R_{xy}^{2\omega}$ is due to the nonlinear current dependence of SOT. When a sample is

subjected to SOT, the magnetization $\mathbf{m}$ deviates as $\mathbf{m}(\theta + \Delta\theta, \phi + \Delta\phi) \approx \mathbf{m}(\theta, \phi) + \frac{d\mathbf{m}(\theta,\phi)}{d\theta}\Delta\theta +$

$\frac{d\mathbf{m}(\theta,\phi)}{d\phi}\Delta\phi + \frac{1}{2}\frac{d^2\mathbf{m}(\theta,\phi)}{d\theta^2}(\Delta\theta)^2 + \frac{1}{2}\frac{d^2\mathbf{m}(\theta,\phi)}{d\phi^2}(\Delta\phi)^2 + \cdots$, where $\Delta\theta$ and $\Delta\phi$ are dominated by the DL

and FL SOT fields, respectively (Supplementary Information S1). However, only the linear terms have

been considered in conventional SOT characterization studies in low-current regimes thus far. Given

that the unconventional angular dependency is directly linked to the nonlinear current dependences

including J_0^2 and J_0^3 terms, the observation of unconventional angular dependency indicates that

SOT induces nonlinear magnetization dynamics, as expressed by $(\Delta\theta)^2$, $(\Delta\theta)^3$ and $(\Delta\phi)^2$, $(\Delta\phi)^3$,

and so on. Therefore, our results provide a clue with which to understand SOT-induced magnetization

dynamics during magnetization switching under a high current, which is relevant with regard to device applications in practice.

Conclusion

We systematically investigated the azimuthal angle (ϕ)-dependent harmonic Hall resistances $R_{xy}^{1\omega}$ and $R_{xy}^{2\omega}$ of a Pt/YIG bilayer in a wide current range. Under low-current conditions, we observed conventional ϕ-dependent behavior of $R_{xy}^{1\omega}$ and $R_{xy}^{2\omega}$; the former exhibits $\sin 2\phi$ behavior while the latter consists of $\cos \phi$ and $\cos 3\phi$ terms, associated with damping-like and field-like SOTs, respectively. As the current increases, the ϕ dependencies of $R_{xy}^{1\omega}$ and $R_{xy}^{2\omega}$ deviate significantly from the conventional curves, where higher-order angular-dependent terms become non-negligible, i.e., sizable $\sin 4\phi$ and $\sin 6\phi$ terms in $R_{xy}^{1\omega}$ and the $\cos 5\phi$ and $\cos 7\phi$ terms in $R_{xy}^{2\omega}$. It was found that the magnitude of the 4ϕ (5ϕ) term of $R_{xy}^{1\omega}$ ($R_{xy}^{2\omega}$) could reach 30% (20%) of that of the lowest-order 2ϕ (1ϕ) term at a current density of $J_0 = 2 \times 10^{11}$ A/m^2. Our experimental result is in qualitative agreement with the SOT-related equations of $R_{xy}^{1\omega}$ and $R_{xy}^{2\omega}$ [i.e., Eqs. (1), (2)], suggesting that the unconventional ϕ-dependence of $R_{xy}^{1\omega}$ and $R_{xy}^{2\omega}$ is due to nonlinear current-dependent SOTs. Our result will provide a general method by which to analyze SOT-related harmonic Hall resistance and to comprehend SOT-induced magnetization dynamics during SOT-induced switching under large currents.

Methods

Thin film deposition and sample fabrication. The YIG (30 nm) film in this study was grown on a $Gd_3Ga_5O_{12}$ (GGG) (111) substrate by RF sputtering (200 W) using a customized off-stoichiometric target, followed by a post-thermal treatment at 750°C in an oxygen-rich environment for two hours. The sputtering target was prepared for the composition of Y and Fe of 3:5.03 using the same method as described in the previous work[40]. Sputtering was conducted at a working pressure of 15 mTorr with an Ar and O_2 mixture gas. Then, Pt (3 nm) films were deposited by DC magnetron sputtering with a working pressure of 0.4 Pa and a power of 30 W at room temperature. Hall-bar patterned devices were fabricated by photolithography and ion milling, and electrical contact pads of Cr (5 nm)/Au (70 nm) layers were defined by additional photolithography and lift-off processes.

AC lock-in harmonic measurement. Harmonic measurements were performed with AC current (frequency of 7 Hz) using lock-in amplifiers (SR830) and a source meter (Keithley 6221). Root mean-square values were used for the current values to calculate the resistance values; i.e., $R = V/(I_0/\sqrt{2})$, where I_0 is the amplitude of the AC current $I = I_0 \sin(\omega t)$ and V is the measured voltage.

References

1. Manchon, A. *et al.* Current-induced spin-orbit torques in ferromagnetic and antiferromagnetic systems. *Rev Mod Phys* **91**, 035004 (2019).

2. Garello, K. *et al.* Symmetry and magnitude of spin–orbit torques in ferromagnetic heterostructures. *Nature Nanotechnology* **8**, 587–593 (2013).

3. Ryu, J., Lee, S., Lee, K. J. & Park, B. G. Current-Induced Spin–Orbit Torques for Spintronic Applications. *Advanced Materials* **32**, 1907148 (2020).

4. Aradhya, S. V., Rowlands, G. E., Oh, J., Ralph, D. C. & Buhrman, R. A. Nanosecond-Timescale Low Energy Switching of In-Plane Magnetic Tunnel Junctions through Dynamic Oersted-Field-Assisted Spin Hall Effect. *Nano Lett* **16**, 5987–5992 (2016).

5. Baumgartner, M. *et al.* Spatially and time-resolved magnetization dynamics driven by spin–orbit torques. *Nature Nanotechnology* **12**, 980–986 (2017).

6. Ryu, K. S., Thomas, L., Yang, S. H. & Parkin, S. Chiral spin torque at magnetic domain walls. *Nature Nanotechnology* **8**, 527–533 (2013).

7. Emori, S., Bauer, U., Ahn, S. M., Martinez, E. & Beach, G. S. D. Current-driven dynamics of chiral ferromagnetic domain walls. *Nature Materials* **12**, 611–616 (2013).

8. Garello, K., Yasin, F. & Kar, G. S. Spin-orbit torque MRAM for ultrafast embedded memories: From fundamentals to large scale technology integration. *2019 IEEE 11th International Memory Workshop, IMW* (2019).

9. Yang, S. H., Garg, C., Phung, T., Rettner, C. & Hughes, B. Spin-orbit torque driven one-bit magnetic racetrack devices-memory and neuromorphic applications. *2019 International Symposium on VLSI Technology, Systems and Application, (VLSI-TSA)* (2019).

10. Haidar, M. *et al.* A single layer spin-orbit torque nano-oscillator. *Nature Communications* **10**, 1–6 (2019).

11. Choi, J. G. *et al.* Voltage-driven gigahertz frequency tuning of spin Hall nano-oscillators. *Nature Communications* **13**, 1–8 (2022).

12. Kim, Y., Fong, X. & Roy, K. Spin-Orbit-Torque-Based Spin-Dice: A True Random-Number Generator. *IEEE Magn Lett* **6**, (2015).

13. Wimmer, T. *et al.* Spin Transport in a Magnetic Insulator with Zero Effective Damping. *Phys Rev Lett* **123**, 257201 (2019).

14. Zhou, J. *et al.* Spin–Orbit Torque-Induced Domain Nucleation for Neuromorphic Computing. *Advanced Materials* **33**, 2103672 (2021).

15. Sinova, J., Valenzuela, S. O., Wunderlich, J., Back, C. H. & Jungwirth, T. Spin Hall effects. *Rev Mod Phys* **87**, 1213–1260 (2015).

16. Edelstein, V. M. Spin polarization of conduction electrons induced by electric current in two-dimensional asymmetric electron systems. *Solid State Commun* **73**, 233–235 (1990).

17. Haney, P. M., Lee, H. W., Lee, K. J., Manchon, A. & Stiles, M. D. Current induced torques and interfacial spin-orbit coupling: Semiclassical modeling. *Phys Rev B Condens Matter Mater Phys* **87**, 174411 (2013).

18. Liu, L. *et al.* Spin-torque switching with the giant spin hall effect of tantalum. *Science* **336**, 555–558 (2012).

19. Ou, Y., Ralph, D. C. & Buhrman, R. A. Strong Enhancement of the Spin Hall Effect by Spin Fluctuations near the Curie Point of FexPt1-x Alloys. *Phys Rev Lett* **120**, 097203 (2018).

20. Wen, Y. *et al.* Temperature dependence of spin-orbit torques in Cu-Au alloys. *Phys Rev B* **95**, 104403 (2017).

21. MacNeill, D. *et al.* Control of spin–orbit torques through crystal symmetry in WTe2/ferromagnet bilayers. *Nature Physics* **13**, 300–305 (2016).

22. Li, P. *et al.* Spin-momentum locking and spin-orbit torques in magnetic nano-heterojunctions composed of Weyl semimetal WTe2. *Nature Communications* **9**, 1–10 (2018).

23. Han, J. *et al.* Roomerature Spin-Orbit Torque Switching Induced by a Topological Insulator. *Phys Rev Lett* **119**, 077702 (2017).

24. Wang, Y. *et al.* Room temperature magnetization switching in topological insulator-ferromagnet heterostructures by spin-orbit torques. *Nature Communications* **8**, 1–6 (2017).

25. Fan, Y. *et al.* Magnetization switching through giant spin–orbit torque in a magnetically doped topological insulator heterostructure. *Nature Materials* **13**, 699–704 (2014).

26. Nguyen, M. H. & Pai, C. F. Spin-orbit torque characterization in a nutshell. *APL Mater* **9**, 30902 (2021).

27. Nakayama, H. *et al.* Spin Hall Magnetoresistance Induced by a Nonequilibrium Proximity Effect. *Phys Rev Lett* **110**, 206601 (2013).

28. Meyer, S. *et al.* Anomalous Hall effect in YIG|Pt bilayers. *Appl Phys Lett* **106**, 132402 (2015).

29. Li, Y. *et al.* Current-Induced Magnetization Switching Across a Nearly Room-Temperature Compensation Point in an Insulating Compensated Ferrimagnet. *ACS Nano* **16**, 8181–8189 (2022).

30. Liu, G. *et al.* Magnonic Unidirectional Spin Hall Magnetoresistance in a Heavy-Metal-Ferromagnetic-Insulator Bilayer. *Phys Rev Lett* **127**, 207206 (2021).

31. Kang, M. G. *et al.* Electric-field control of field-free spin-orbit torque switching via laterally modulated Rashba effect in Pt/Co/AlOx structures. *Nature Communications* **12**, 1–8 (2021).

32. Lee, S. *et al.* Efficient conversion of orbital Hall current to spin current for spin-orbit torque switching. *Communications Physics* **4**, 1–6 (2021).

33. Avci, C. O. *et al.* Interplay of spin-orbit torque and thermoelectric effects in ferromagnet/normal-metal bilayers. *Phys Rev B Condens Matter Mater Phys* **90**, 224427 (2014).

34. Cheng, Y. *et al.* Third harmonic characterization of antiferromagnetic heterostructures. *Nature Communications* **13**, 1–6 (2022).

35. Chen, Y. T. *et al.* Theory of spin Hall magnetoresistance. *Phys Rev B Condens Matter Mater Phys* **87**, 144411 (2013).

36. Huang, S. Y. *et al.* Transport magnetic proximity effects in platinum. *Phys Rev Lett* **109**, 107204 (2012).

37. Lu, Y. M. *et al.* Pt magnetic polarization on Y3Fe5O12 and magnetotransport characteristics. *Phys Rev Lett* **110**, 147207 (2013).

38. Ding, J. *et al.* Nanometer-Thick Yttrium Iron Garnet Films with Perpendicular Anisotropy and Low Damping. *Phys Rev Appl* **14**, 014017 (2020).

39. Zhang, S. S. L. & Vignale, G. Nonlocal Anomalous Hall Effect. *Phys Rev Lett* **116**, 136601 (2016).

40. Cao Van, P. *et al.* Effect of annealing temperature on surface morphology and ultralow ferromagnetic resonance linewidth of yttrium iron garnet thin film grown by rf sputtering. *Appl Surf Sci* **435**, 377–383 (2018).

Competing financial interests

The authors declare no conflict of interest.

Author contributions

T.S. and B.-G.P. initiated this study. T.S. and G.K. fabricated the devices and performed the harmonic Hall measurements. T.S. and J.-G.C. analyzed the data and derived the equations. P.C.V. and J.-R.J. prepared the YIG thin film. T.S. and B.-G.P. wrote the manuscript with the help of all authors

Data availability

The data that support the findings of this study are available from the corresponding author upon reasonable request.

Additional Information

Supplementary information is available in the online version of the paper. Reprints and permissions information is available online at www.nature.com/reprints. Correspondence and requests for materials should be addressed to B.-G.P
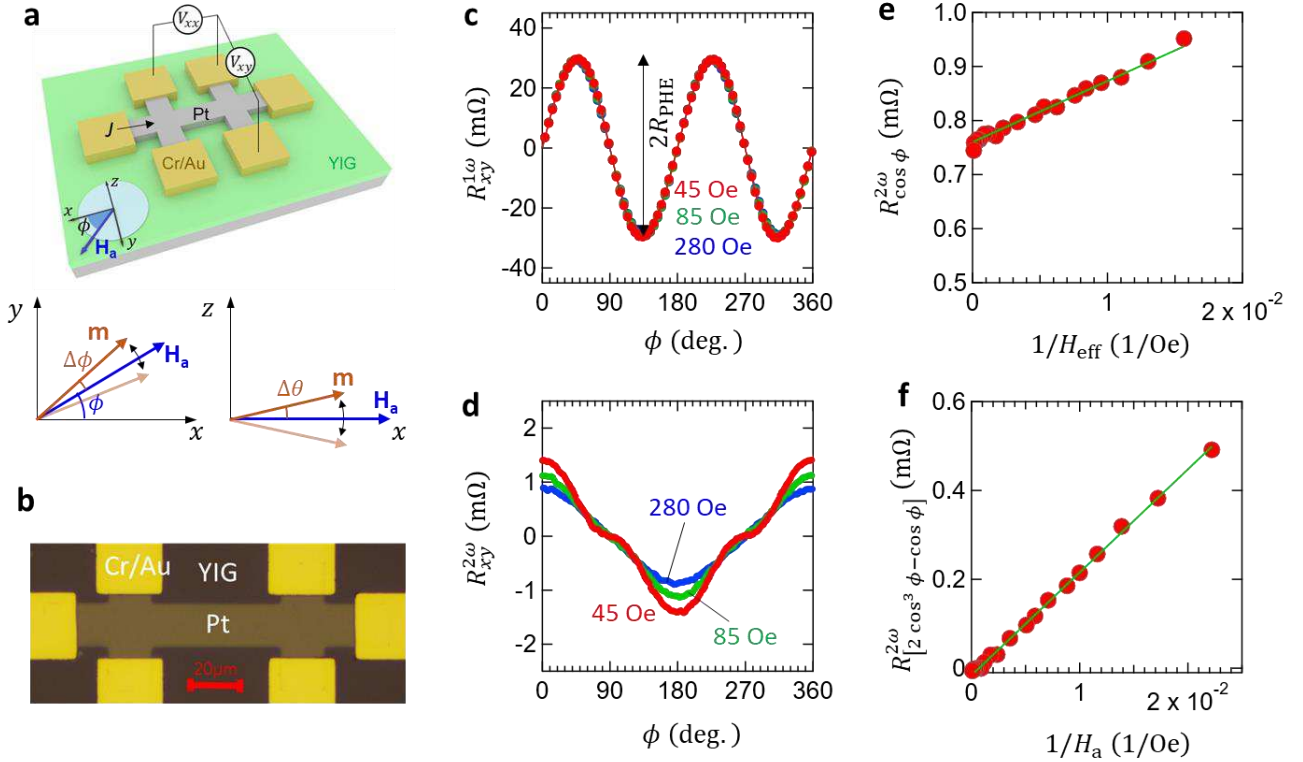
Figure 1 | Harmonic Hall resistances $R_{xy}^{1\omega}$ and $R_{xy}^{2\omega}$ of a Pt/YIG structure under a low-current regime. a, b, Schematic illustration (**a**) and optical microscopy image (**b**) of the Pt (3 nm)/YIG (30 nm) Hall-bar sample. The bottom of Fig. 1**a** indicates the SOT-induced oscillation of magnetization **m** with a modulation amplitude of $(\Delta\theta, \Delta\phi)$ around a magnetic field (H_a). Current is injected in the *x* direction. An external magnetic field H_a is applied on the *x-y* plane. **c, d,** Angular dependences of $R_{xy}^{1\omega}$ (**c**) and $R_{xy}^{2\omega}$ (**d**) measured at $H_a = 45$, 85 and 280 Oe. Note that constant offsets are subtracted from the $R_{xy}^{1\omega}$ and $R_{xy}^{2\omega}$ plots. **e, f,** $R_{\cos\phi}^{2\omega}$ (**e**) and $R_{[2\cos^3\phi-\cos\phi]}^{2\omega}$ (**f**) as a function of $1/H_{\text{eff}}$ and $1/H_a$, respectively. The solid lines indicate the linear fitting results. The data for **c-f** were obtained at $J_0 = 8.3 \times 10^{10}$ A/m^2.
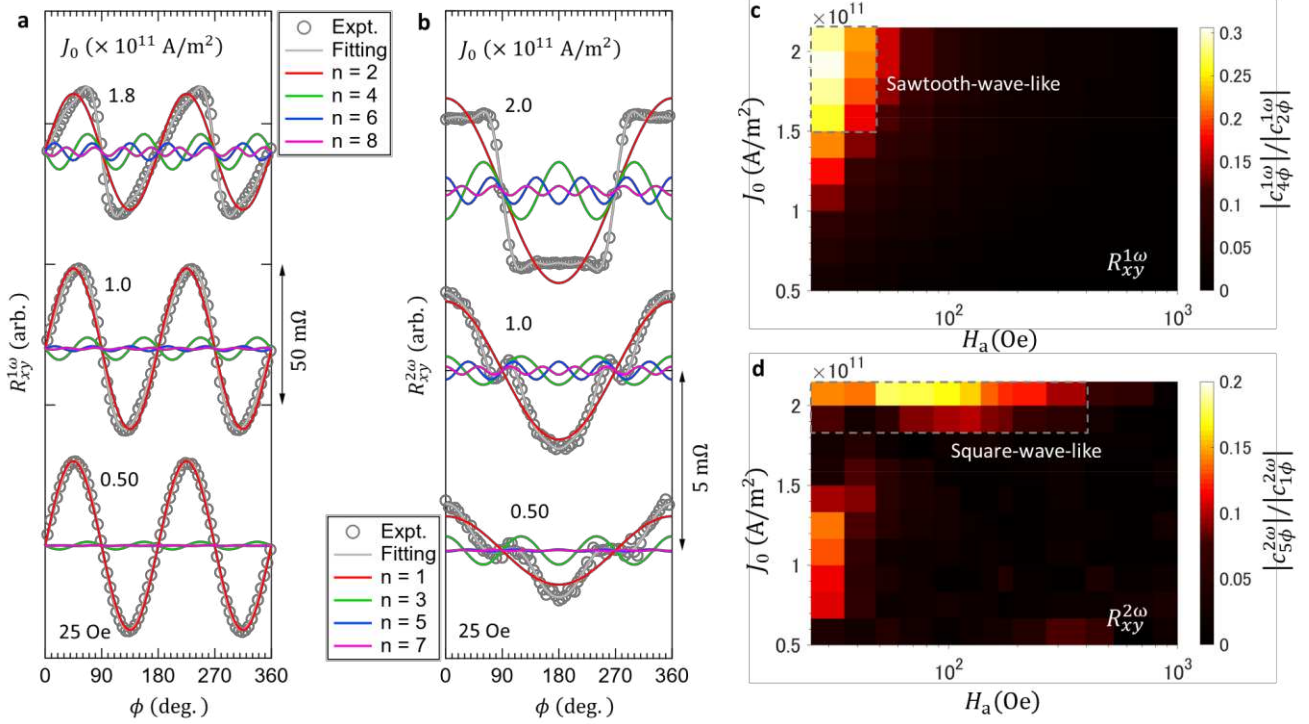
Figure 2 | $R_{xy}^{1\omega}$ and $R_{xy}^{2\omega}$ for various values of current density and magnetic fields.

a, b, Angular dependences of $R_{xy}^{1\omega}$ (**a**) and $R_{xy}^{2\omega}$ (**b**) at H_a = 25 Oe for three different current densities. The grey solid curve indicates the fitting result, and the curves shown in red, green, blue and pink indicate the $c_{n\phi}\sin(n\phi)$ (n = 2,4,6,8) components of $R_{xy}^{1\omega}$ (**a**) and the $c_{n\phi}\cos(n\phi)$ (n = 1,3,5,7) components of $R_{xy}^{2\omega}$ (**b**), as obtained from fitting using Eqs. (1) and (2). **c, d**, the J_0-H_a diagrams of absolute values of the lowest-order unconventional angular-dependent coefficients, $\left|c_{4\phi}^{1\omega}\right|$ (**c**) and $\left|c_{5\phi}^{2\omega}\right|$ (**d**), normalized by the leading terms $\left|c_{2\phi}^{1\omega}\right|$ and $\left|c_{1\phi}^{2\omega}\right|$, respectively.
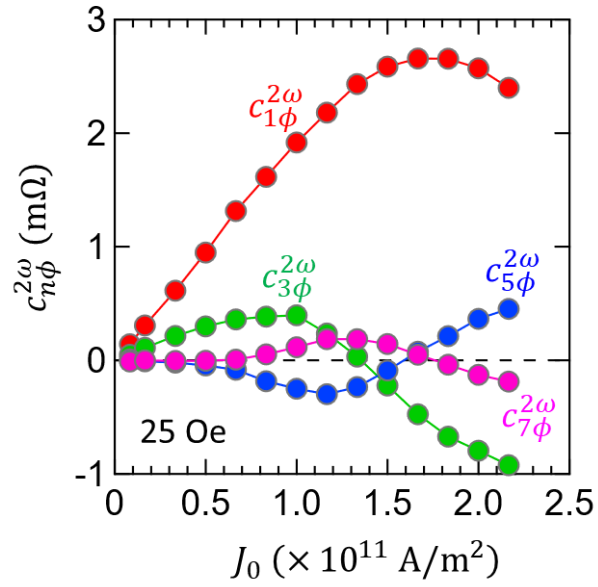
Figure 3 | Current-density dependence of the coefficients $c_{n\phi}^{2\omega}$ ($n = 1, 3, 5, 7$).

$c_{n\phi}^{2\omega}$ were obtained by fitting the $R_{xy}^{2\omega}$ data at H_a = 25 Oe to Eq. (2).

Supplementary Files

This is a list of supplementary files associated with this preprint. Click to download.

- SMfinal.docx